



A three-dimensional numerical model of a micro laminar flow fuel cell with a bridge-shaped microchannel cross-section



Pedro O. Lopez-Montesinos, Amit V. Desai, Paul J.A. Kenis^{*}

Department of Chemical & Biomolecular Engineering, University of Illinois at Urbana-Champaign, 600 South Matthews Ave, Urbana, IL 61801, USA

HIGHLIGHTS

- The developed 3D numerical model was in excellent agreement with experimental data.
- Lower flow rates lead to higher peak power density and fuel utilization.
- A bridge-shaped microchannel design increases reactant use and improves cell performance.
- Lower aspect ratio bridge structure leads to higher peak power density.

ARTICLE INFO

Article history:

Received 29 March 2014

Received in revised form

13 June 2014

Accepted 19 June 2014

Available online 7 July 2014

Keywords:

Membraneless fuel cell

Laminar flow fuel cell

Numerical model

Convection-diffusion equations

Electrode kinetics equations

COMSOL

ABSTRACT

The operation of a laminar flow fuel cell (LFFC) involves complex interplay between various mass and electrochemical transport processes. Hence, to better design and more accurately predict performance, we developed a fully-coupled 3D numerical model that includes all the transport processes and electrochemical phenomena. Specifically, the model is based on the equations for the mass, momentum, species, and charge balances along with Butler–Volmer equations for electrode kinetics. The developed model was in excellent agreement with experimental data on a micro laminar flow fuel cell (μ LFFC) with a bridge-shaped microchannel cross-section. Then, we used the model for a parametric study evaluating the influence of different operational and geometrical parameters (bridge aspect ratio, reactant flow rates, oxidant concentration) on the fuel cell performance (peak power density, fuel crossover, crossover current, power losses). The observed correlations were explained on the basis of mass and electrochemical transport phenomena, e.g., the behavior of the depletion zones at the fuel–oxidant and reactant–electrode interfaces. Based on these results, we recommend further design considerations for LFFCs. Although, the model was specifically developed for a particular μ LFFC configuration, the computational model can be used to design and predict behavior of a wide variety of LFFC configurations.

© 2014 Elsevier B.V. All rights reserved.

1. Introduction

Recently on-chip integrated micro-fuel cells as alternative power sources for portable technologies and lab-on-a-chip devices with extremely small form factor have received increasing attention [1,2] with potential applications in a variety of technologies, e.g., biomedical micro-devices, micro-vehicles, micro-robots [3–10]. Additionally, co-fabrication of the power source along with other electronic components on the same device will enable miniaturization of devices, reductions in weight and cost, improved signal integrity, and minimum number of interconnects [11,12]. Laminar flow fuel cells (LFFCs), which significantly simplify the

micro-fuel cell architecture by eliminating the proton exchange membrane (PEM), have motivated researchers to explore beyond purely miniaturization efforts and also focus on on-chip integration [7,13]. By excluding the PEM, the traditional micro-fuel cell stack (i.e., the bipolar plates and the membrane electrode assembly) coalesces into a single substrate, enhancing the possibility of full on-chip monolithic integration with fabrication processes derived from the MEMS and IC industries.

LFFCs exploit the characteristics of laminar flow at the micro-scale to separate the co-flowing fuel and oxidant streams within a single channel [14]. The diffusion along the interface can be controlled and, hence the fuel crossover can be minimized while still allowing proton transport. This micro-fuel cell configuration significantly reduces ohmic losses associated with the PEM, as well as the electro-osmotic drag and water management issues (i.e., hydration/dehydration cycles and cathode flooding) [14,15]. Along

^{*} Corresponding author. Tel.: +1 217 265 0523; fax: +1 217 333 5052.

E-mail address: kenis@illinois.edu (P.J.A. Kenis).

with the appropriate choice of fuel and oxidants, the performance of a LFFC can be optimized by tuning the various geometrical and operational parameters. As a result, researchers [10,14,16–20] have explored different geometries to improve the performance of LFFCs with respect to power density, fuel utilization, reduced losses etc. Although these studies have yielded improved LFFC performance, tremendous scope still exists to further enhance the performance so that LFFC is a commercially-competitive technology. For optimal design and performance of LFFCs, analytical and computational modeling is required that will enable (1) better understanding of the mechanisms and the relationships between the various geometrical, operational and electrochemical parameters, (2) improved prediction of the fuel cell performance, and (3) reduced number of expensive, tedious, and challenging experimental trials.

Motivated by this need for analytical and computational modeling, several reports in literature exist on modeling of LFFCs focusing on various aspects [16,18,21–28]. As air is being explored as a source of oxygen for LFFCs, the transport of gases at the cathode have been modeled to study the effect of oxygen availability on the electrode performance [26,28]. In another report, researchers studied the influence of flow modification, which was induced by chaotic advection, on mass transport of fuel and oxidants, and subsequently on the performance of the cell [27]. Majority of the computational studies in literature related to LFFCs have focused on the effects of geometry, fuel and electrolyte flow rates, and the relationship between geometry and flow rate on the performance of the fuel cell [16,21–24]. Two of these reports have also studied the influence of concentrations of fuel and oxidants [16] and porosity [23] on the overall cell performance. Comprehensive cell-level modeling of LFFC was performed by Krishnamurthy *et al.* [25] and Shaegh *et al.* [18], and the latter group followed up the research with a review paper discussing the various design consideration for membraneless LFFCs, and the effect of electrode structure and their arrangements on cell performance, fuel crossover, and fuel utilization [2].

Here, we present computational models for LFFCs that are similar to those reported earlier, but focusing on the on-chip integrated micro laminar flow fuel cell (μ LFFC) developed by our group [13]. Specifically, we developed a three dimensional (3D) numerical model to study the effect of the various physicochemical and electrochemical parameters in an operating micro-fuel cell on its overall performance. First, we discuss a simplified version of the model where electrochemical reactions are excluded from the system, which enabled us to inspect the behavior of the mixing zone and quantify fuel crossover for different channel geometries and upstream flow conditions (*i.e.*, reactant flow rate and concentration). Then, we discuss a complete fuel cell model that couples all the transport and electrochemical processes that occur within a working μ LFFC. Based on these models, we propose new cell designs and operating parameters. Although the model was developed for a specific LFFC configuration [13], the model can be applied for theoretical characterization, optimization and performance prediction of different LFFC configurations.

2. Details of the fuel cell model

2.1. Geometry definition

The main reason for using a bridge-shaped microchannel geometry for our micro laminar flow fuel cell (μ LFFC) [13] is to minimize the fuel-to-oxidant diffusive contact and isolate the mixing zone from the electrode areas while enabling efficient proton transport. A bridge-shaped microchannel cross-section provides more walls for electrode integration, thus increasing the reactive area. This configuration enabled the electrochemical

reactions at the anode and cathode to proceed more efficiently as minimal or no interaction between the mixing region and the reaction zones was observed in the simulations. Fig. 1 illustrates the top and cross-sectional views of the microchannel structure along with the various geometrical parameters. In our analyses, three different aspect ratios (ARs) for the bridge structure were considered (AR 10, AR 5, and AR 4), where AR is defined as the ratio of the bridge width (100 μ m) to the bridge height (X in Fig. 1).

2.2. Mixing zone model

We initially developed a simplified model of the fuel cell (mixing zone model) to study the behavior of the mixing zone, quantify fuel crossover and obtain an initial estimate of the geometrical and operational parameters. This model does not include the electrochemical reactions. We used a commercial finite-element-method (FEM) software, COMSOL Multiphysics 3.4 (COMSOL, Stockholm, Sweden) to develop a three dimensional (3D) model of the fuel cell. The fuel (formic acid) and oxidant (potassium permanganate) streams enter separately through a Y-shaped entrance (Fig. 1(A)), merge at the bridge location, and flow in parallel towards the exit. The computational domain consisted of two sub-domains – the anodic and the cathodic flow channels – that allowed us to assign different physical properties and input conditions for each stream. The simplified version of the model does not include the sub-domains corresponding to the catalyst layers and current collectors. The values for the physical properties and the input parameters for the simulations are listed in Supplementary information (SI). The various assumptions, governing equations, boundary conditions, and the procedure for fuel crossover quantification are discussed in SI. Briefly, the steady-state Navier–Stokes and the convection–diffusion equations were solved to obtain the velocity and concentration fields. Then an artificial boundary was included to quantify the fuel crossover.

2.3. Fuel cell model

To assess the I–V characteristics (*i.e.*, performance) of the μ LFFCs via numerical simulations, the mixing zone model described in the previous sub-section was extended to include the electrochemical reactions. Specifically, the voltage profile was estimated due to the current generated at the electrodes when the cell is in operation, and the charge balance and Butler–Volmer equations were coupled to obtain a complete model of the fuel cell.

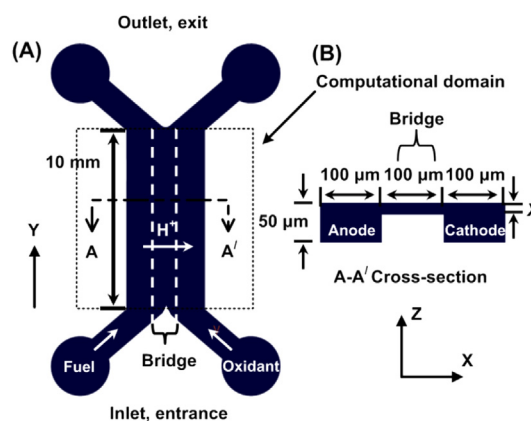


Fig. 1. Schematic illustration of the (A) top view, and (B) cross-sectional view of the bridge-shaped microchannel structure. The values of the various geometrical parameters used in the simulations are shown in the figure, where X is 10, 20 and 25 μ m.

To complete the fuel cell model, two new sub-domains were added to account for additional physics: the anodic and cathodic porous electrodes. The reactants, the fuel (formic acid in this case) and the oxidant (potassium permanganate in this case), flow through the anodic and cathodic micro flow channels, respectively, come into superficial contact with the porous electrodes, where the electrochemical reactions occur, but do not flow through these sub-domains. The electrodes were modeled as porous sub-domains that include the catalyst layer (*i.e.*, palladium) and the current collector (*i.e.*, gold) lumped together.

The various assumptions, governing equations, boundary conditions, and the procedures for including electrochemical reactions, estimation of I–V curves, and quantification of fuel cell performance are discussed in SI. Briefly, the steady-state Navier–Stokes and the convection–diffusion equations were solved to obtain the velocity and concentration fields. To estimate the current, the amount of fuel and oxidant consumed at the anode and cathode electrode walls was quantified using Faraday's Law. To model the porous electrodes, the relevant sub-domains were assumed to be saturated with liquid electrolyte and the effective conductivity was estimated using Archie's law [29,30]. Finally, the current was quantified using Butler–Volmer equations, which describe the dependence of electrical current at the electrode on the electrode potential. The polarization or I–V curves were determined for different aspect ratios of the bridge structure, different flow rates and different oxidant concentrations. Then, the fuel cell performance was characterized based on I–V curves, fuel utilization, power losses, and fuel and oxidant crossover. The physical properties and input parameters used in the simulations are included in SI.

3. Results and discussion

3.1. Velocity field and mixing zone analysis

To study the behavior of mixing zone, the velocity and concentration fields were analyzed for different volumetric flow rates of the fuel and different aspect ratios of the bridge. We ensured that the flow in all simulations cases was laminar, *i.e.* Reynolds number (Re) < 2000 (the maximum Re was 40 in the case of AR 4, $60 \mu\text{L min}^{-1}$). The axial velocity profiles for these different parameters are shown and discussed in SI. For all the conditions, a double-parabolic flow developed with a nearly constant low-velocity field in the bridge region (Fig. S5). The flow profile is not unaffected significantly for different flow rates and aspect ratios. The 3D and 2D concentration profiles for the fuel in case of AR 10 μLFFC are shown and discussed in SI. These profiles indicate that the mixing or depletion zones at the fuel–oxidant interface are distant from the electrode walls, demonstrating that the bridge geometry enables decoupling of the mixing and electrochemical analyses. The mixing zone width can be controlled by adjusting flow rates [16,22]. To illustrate this point, the concentration profiles of the fuel for different flow-rates and different aspect ratios are shown and discussed in SI. Based on the plots, the use of higher flow rates and/or lower bridge aspect ratios will reduce the width of the mixing zone, which in turn will minimize the interaction between the mixing zone and the electrodes. This minimal interaction is expected to improve electrode performance and fuel utilization.

Fig. 2(A), (B) and (C) depicts the width of the mixing zone (Δx) as a function of the axial distance for different aspect ratios. The width increases as the reactants flow towards the exit, but is mostly constrained within the bridge region for all the flow rates. Additionally, the width of the mixing zone decreases as the flow rate increases and the bridge aspect ratio decreases. Fig. 2(D) also

depicts the fuel crossover as a function of fuel flow rate for different aspect ratios. In all the cases, the fuel crossover is very small, maximum being 1.2% for the lowest aspect ratio and lowest flow rate. Péclet number (Pe) characterizes the ratio between advection and diffusion; typically a higher Pe would indicate smaller diffusive zones. Hence, the (diffusive) fuel crossover can be reduced by increasing Pe [16], but increasing Pe by increasing the mean velocity may cause the streams to deviate from the steady state. Such an onset of hydrodynamic instability has been reported in laboratory experiments and may hampers the performance of LFFCs significantly [14]. The plots in Fig. 2 also imply that the aspect ratio has opposing effects on the width of the mixing zone and fuel crossover. In summary, the use of higher flow rates and/or lower bridge aspect ratios will reduce the width of the diffusion zone, which reduces the diffusive crossover of the fuel. This reduced fuel crossover will improve the electrode performance, which may increase the fuel utilization. These results on relation between flow rates and width of diffusion zone are in agreement with the scaling analysis [22], which indicates that increasing the average velocity results in a thinner diffusion zone.

3.2. Validation of complete fuel cell model

To validate the complete fuel cell model, we calculated the values for the polarization and power-density curves using COMSOL simulations and compared these results with our previous experimental observations for a AR 10 μLFFC (Fig. 3) [13]. The plots show the performance of the cell when operated with 1 M HCOOH and 144 mM KMnO_4 at a flow rate of $60 \mu\text{L min}^{-1}$. The plot confirms that the whole fuel cell model agrees excellently with the experimental data. At low potentials the model performance prediction departs slightly from the experimental data, probably due to the occurrence of secondary reduction reactions. In acidic solutions, the permanganate reduction reaction is prone to yield insoluble MnO_2 at low potentials (<0.5 V). Therefore, mass transport issues at the cathode will limit the overall performance at low potentials as indicated by the experimental polarization curve. Since the fuel cell model does not account for alternative electrochemical reduction pathways, the model predictions deviates from experimental observations at low potentials. However, in practical applications, fuel cells are operated at a nominal voltage of (~ 0.6 – 0.8 V) where the model predictions are in excellent agreement with experimental data. Therefore, all the simulations reported in the remainder of the paper were performed at operating voltages above 0.5 V.

3.3. Cell performance

Since the μLFFCs are cathode-limited, we analyze the performance of the fuel cell with relation to the concentration fields of the oxidant. In SI, we depict the concentration fields in 3D and 2D for a typical simulation. We observed similar behavior for the depletion zone at the fuel–oxidant interface predicted by the fuel cell model to the behavior predicted by the mixing zone model, *i.e.*, the thickness of the depletion zone increases downstream and increasing the flow rate decreases the thickness. We performed the simulations for three different aspect ratios of the bridge (AR 10, 5, 4), various flow rates of the reactants (10 – $60 \mu\text{L min}^{-1}$), and lower and higher concentrations of the oxidant (20 mM and 144 mM), potassium permanganate in this case. Fig. 4 depicts the 2D maps of the oxidant concentration profiles for various parameters, 9 mm downstream from the inlet (close to the outlet), which will be used to correlate to the fuel cell performance. The reason for the almost symmetric concentration profile for the oxidant is due to the assumption of uniform rate of oxidant consumption (depletion) at the cathodic electrode surfaces. This symmetry is more distorted

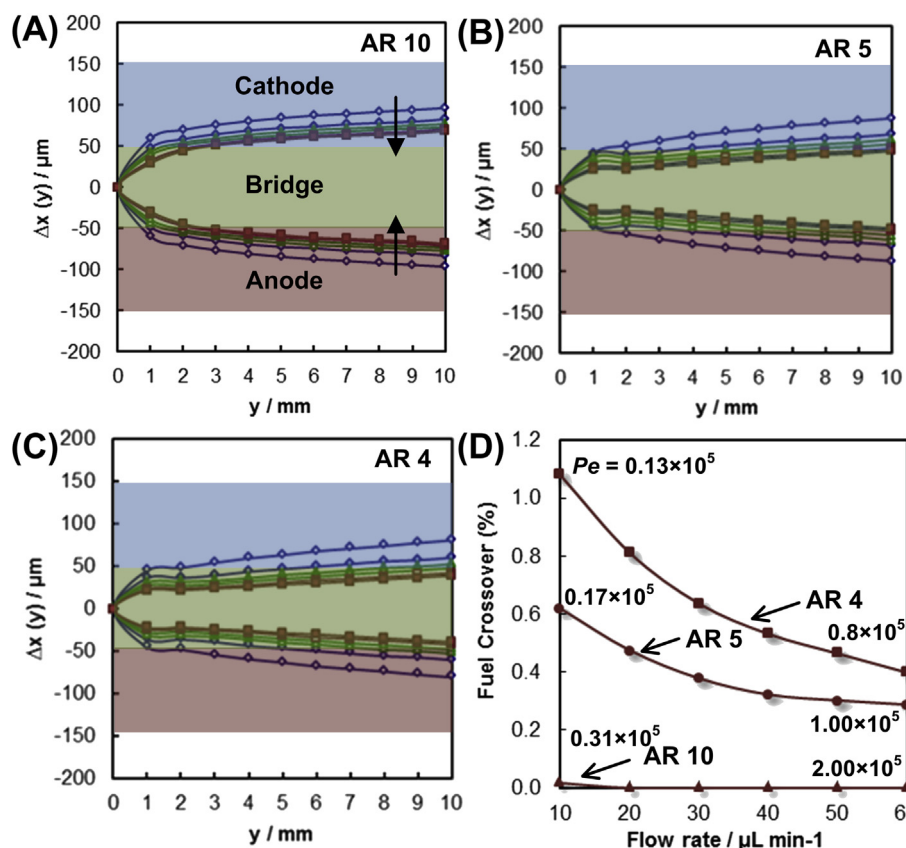


Fig. 2. Plots of mixing zone width (Δx) vs. axial distance for AR 10 (A), AR 5 (B), and AR 4 (C), and plot of fuel crossover vs. flow rate for different aspect ratios (D) of the bridge structure as predicted by the model. The flow rates were 10, 20, 30, 40, 50, and 60 $\mu\text{L min}^{-1}$ and increases in the direction of the arrow. The Péclet number (Pe) for minimum and maximum flow rate are indicated in the fuel crossover plot (D).

for lower aspect ratios and higher flow rates, where the depletion at the oxidant–fuel interface dominates the depletion at the channel boundaries due to oxidant consumption at the electrodes (Fig. 4(E)). Fig. 5 shows polarization and power-density curves for various parameters, which will be used to characterize the fuel cell performance. To illustrate the effect of various parameters on the overall cell performance, we plot the peak power density as a

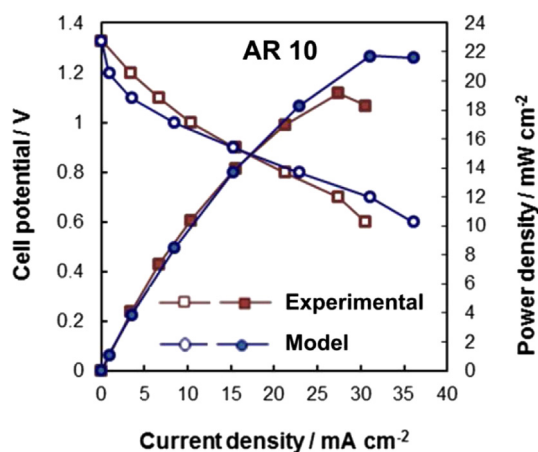


Fig. 3. Polarization (open squares and circles) and power-density (filled squares and circles) curves for the AR10 cell structure when operating with 1 M HCOOH and 144 mM KMnO_4 at a flow rate of 60 $\mu\text{L min}^{-1}$. The model (blue curves) is compared with the experimental data. (For interpretation of the references to color in this figure legend, the reader is referred to the web version of this article.)

function of different parameters in Fig. 6. We report results only for the lowest and highest flow rate, i.e., 10 and 60 $\mu\text{L min}^{-1}$.

For the AR 10 cell structure, the model predicted a peak power density of ~ 13 and $\sim 17 \text{ mW cm}^{-2}$ at flow rates of 10 and 60 $\mu\text{L min}^{-1}$, respectively (Fig. 5(A)). For this specific case, an increase in reactant flow rate improved the overall cell performance. This increase in power density may result from the thinner depletion regions at the reactant–electrode interface at higher flow rates (Fig. 4), which will enhance the reactant transport to the active walls of the cell as the concentration gradients become steeper [18]. In contrast, the performance drops considerably for the lower flow rate case (Fig. 5(A), (B)), where a thicker depletion layer exists (Fig. 4). This drop is evidenced by inspecting the mass transport region of the I–V curves for the lower flow rate case. When a thicker depletion layer is formed, not only the oxidant available in the cathodic microchannel is low but sufficient oxidant does not reach the active walls of the channel as the concentration gradient is low. Therefore, the overall cell performance can be improved by operating the cell at higher flow rate (60 $\mu\text{L min}^{-1}$ in this case).

For a higher oxidant concentration, the model predicted peak power densities of ~ 18 and $\sim 22 \text{ mW cm}^{-2}$ at flow rates of 10 and 60 $\mu\text{L min}^{-1}$ (Fig. 5(B)), respectively, which is higher than those for lower oxidant concentration. This increase in power density may again be attributed to thinner depletion regions resulting from steeper concentration gradients at higher oxidant concentrations. Steeper concentration gradients enhance the flux of reactant to the electrode walls, which leads to enhanced electrochemical transport.

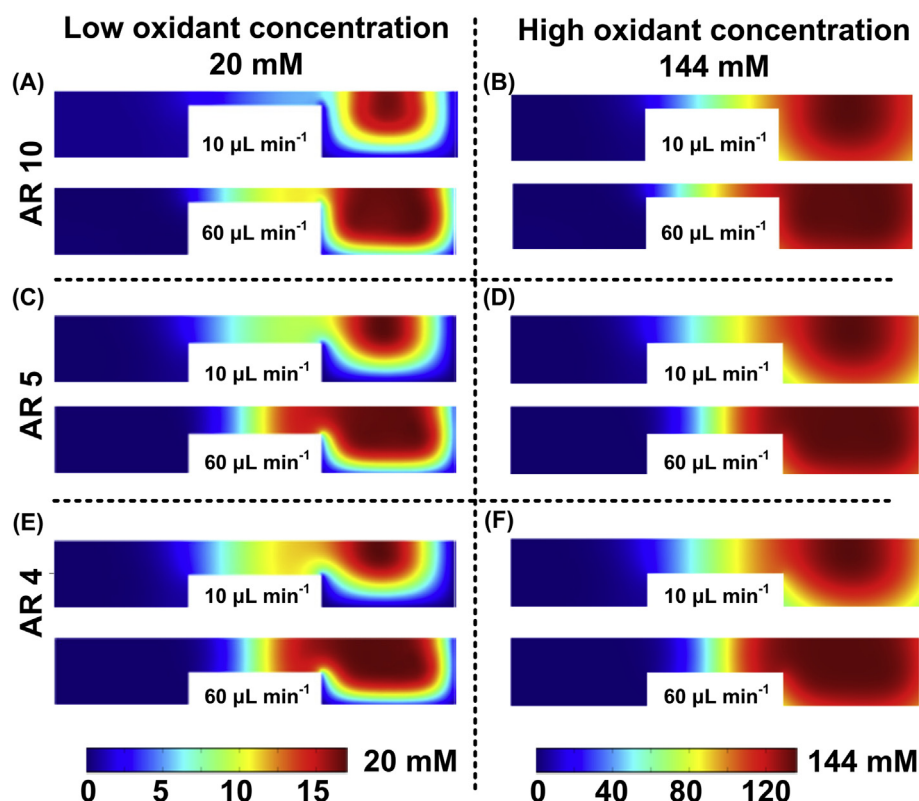


Fig. 4. 2D maps of the concentration profiles of the oxidant as predicted by the model, downstream at 9 mm away from the inlet (close to the outlet), for different aspect ratios of the bridge structure (AR 10, 5, 4), different flow rates (10 and 60 $\mu\text{L min}^{-1}$), and different concentrations of the oxidant, potassium permanganate (20 mM and 144 mM).

For lower aspect ratio of the bridges (AR 5 and 4), we observe similar trends to the AR 10 structure (Fig. 5(C)–(F)), i.e., the cell performance improves with increasing flow rate and oxidant concentration. We also observed that the peak power densities increase with decreasing aspect ratios of the bridge. This observation may be attributed to the reduced cell resistance with lower aspect ratio structures, as larger bridge height (for lower AR) will lead to a bigger aperture for proton transport. However, we expect that if we increase the height of the bridge significantly ($>25 \mu\text{m}$), the inner reactive surface area will decrease, thus hampering cell performance. Fig. 6 also indicates that the improvement in power densities with higher flow rates is not significant for lower aspect ratio structures. Hence, lower flow rates may be preferable for lower aspect ratio structures, as they will result in higher fuel utilization and lower ancillary losses (elaborated in the next sub-section). Overall, the fuel cell performance is governed by the various geometrical and operational parameters that influence the behavior of the depletion zone at the reactant–electrode interface and the proton transport.

3.4. Power losses

3.4.1. Ancillary

Fig. 7 shows the power losses due to active reactant delivery (i.e., the pump), which was determined using the pressure drop simulation results for a range of reactant flow rates and three different aspect ratios of the bridge structure (i.e., AR 10, AR 5, and AR 4). The power losses associated with the active reactant delivery increase with the flow rate, as the pressure drop is proportional to the flow rate (based on the Hagen–Poiseuille equation [31]). Also, as the aspect ratio increases the power losses increase, as the bridge height decreases for higher aspect ratios.

3.4.2. Crossover current

Fig. 8 depicts the crossover current due to the oxidant or fuel reactant crossover for the AR 4 structure at $V_{\text{cell}} = 0.7 \text{ V}$. AR 4 structure was selected for the analysis since it showed the largest fuel crossover based on the mixing zone model (Fig. 2). To estimate the crossover current, we assumed that the fuel that crosses to the cathodic micro flow channel is completely oxidized at the catalyst layer and the oxidant that crosses to the anodic micro flow channel is completely reduced at the catalyst layer. When the cell was operating at a fuel and oxidant concentration of 1 M HCOOH and 144 mM KMnO_4 , respectively at a flow rate of 10 $\mu\text{L min}^{-1}$, crossover currents of 6.0 and 2.4 mA cm^{-2} were estimated due to fuel and oxidant crossover, respectively. Similarly, when the cell operated under the same conditions at higher reactant flow rate (60 $\mu\text{L min}^{-1}$), crossover currents were 6.4 and 5.5 mA cm^{-2} . We observed that the crossover current due to the fuel is not as strongly dependent on the flow rate as the crossover current due to the oxidant. The crossover current increases with increasing flow rate, as the oxidant depletion region is more pronounced at the lower flow rate (and also the oxidant consumption as explained later) that decreases the concentration gradient for the oxidant flux to cross to the anodic micro flow channel. When the cell operated at the lower oxidant concentration (20 mM), low crossover currents were observed, 0.3 and 0.78 mA cm^{-2} at flow rates of 10 and 60 $\mu\text{L min}^{-1}$, respectively. This correlation shows that lowering the reactant concentration is an effective way of reducing crossover and consequently crossover current density.

3.4.3. Fuel utilization (at V_{cell})

Fig. 9(A) shows the fuel utilization for the AR 4 structure when operating with 1 M HCOOH at the lowest and highest flow rates (10 and 60 $\mu\text{L min}^{-1}$). Fuel concentration profiles are shown when the

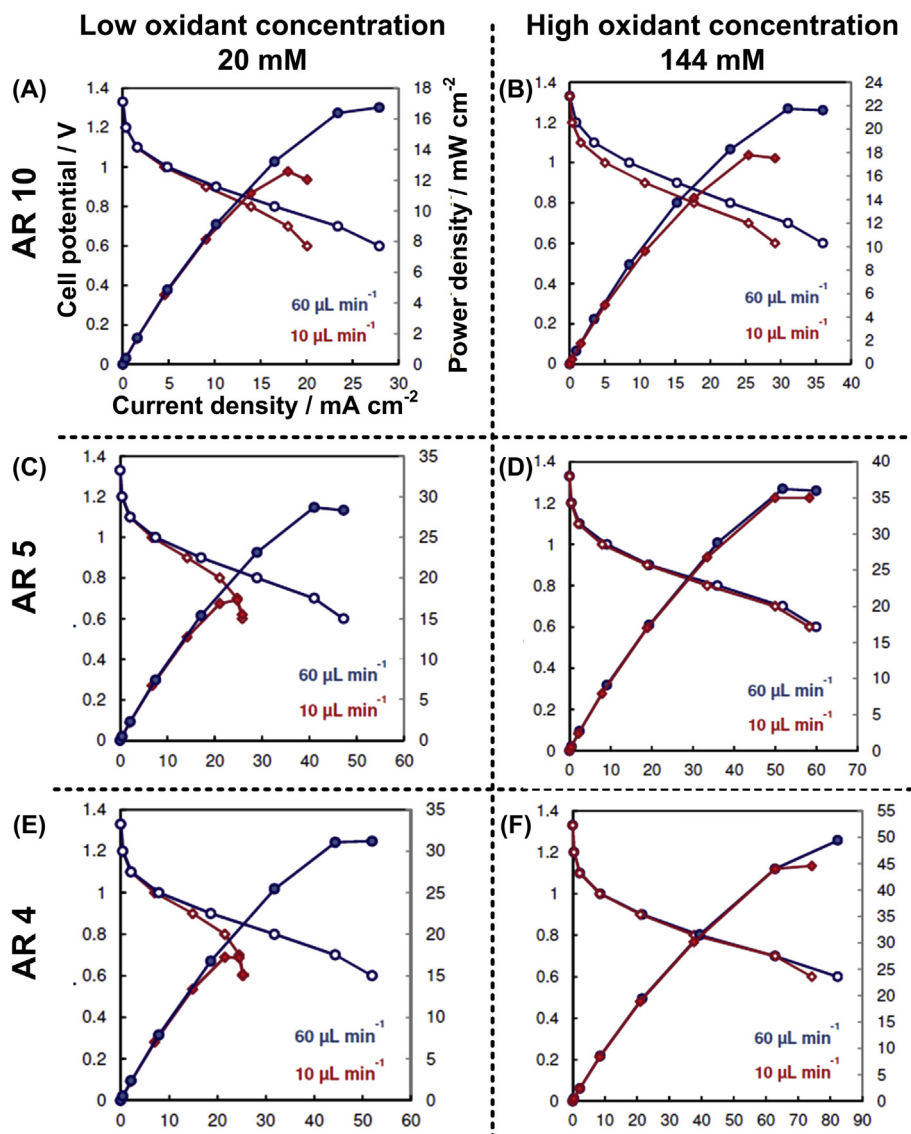


Fig. 5. Polarization (open squares and circles) and power-density (filled squares and circles) curves as predicted by the model for different aspect ratios of the bridge structure (AR 10, 5, 4), different flow rates (10 and 60 $\mu\text{L min}^{-1}$), and different concentrations of the oxidant, potassium permanganate (20 mM and 144 mM).

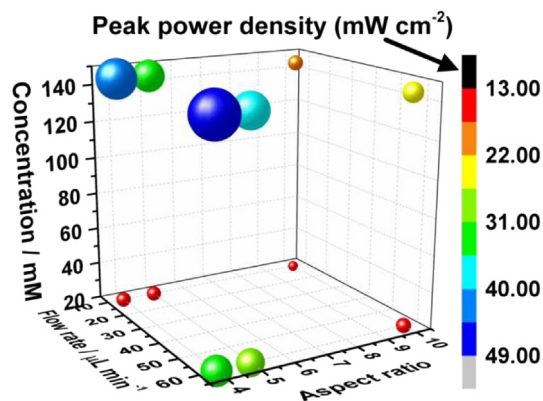


Fig. 6. Plot of peak power density as a function of different geometrical and operational parameters (oxidant concentration, reactant flow rate, and bridge aspect ratio). The sphere size and color indicates the relative value of the power density. (For interpretation of the references to color in this figure legend, the reader is referred to the web version of this article.)

cell operated at the lowest and highest flow rate, 9 mm downstream from the inlet (close to the outlet). When the cell was operating at the lowest and highest flow rate, the fuel utilization was 15.5% and 6.4%, respectively for an inlet fuel concentration of 1 M HCOOH. The lowest flow rate led to increased fuel utilization due to the increased fuel residence time within the reactive anodic micro flow channel. The fuel concentration maps for the highest operating flow rate indicate a modest boundary (depletion) layer, which explains the low fuel utilization. However, our cell is cathode-limited, which means that the produced current will balance according to the cathode reaction kinetics. Therefore, the cell cannot be optimized by increasing the fuel concentration, but the fuel utilization can be greatly improved by decreasing the fuel concentration.

3.4.4. Oxidant consumption rate (at V_{cell})

Fig. 9(B) shows the oxidant consumption rate for the AR 4 structure when operating at the lowest and highest reactant flow rate (10 and 60 $\mu\text{L min}^{-1}$) and lower and higher oxidant concentration (20 and 144 mM). At the higher and lower operating

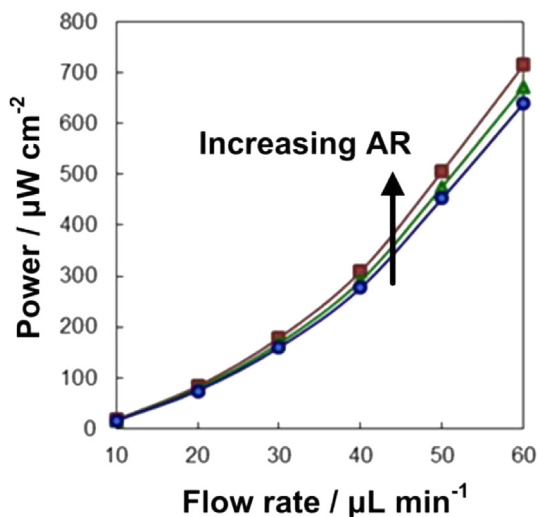


Fig. 7. Power losses ($\mu\text{W cm}^{-2}$) due to the active reactant delivery (i.e., pump) determined from the cell pressure drop for various flow rates (10, 20, 30, 40, 50, and $60 \mu\text{L min}^{-1}$) and three different aspect ratios of the bridge structure (AR 10, AR 5, and AR 4).

concentration, the oxidant consumption is 28% and 62%, respectively, at a flow rate of $10 \mu\text{L min}^{-1}$. Similarly, the oxidant consumption is 18% and 6% at a flow rate of $60 \mu\text{L min}^{-1}$. Lower flow rate will lead to increased oxidant consumption due to the increased oxidant residence time within the reactive cathodic micro flow channel. Also, the lower oxidant concentration shows increased oxidant consumption compared to the higher oxidant concentration, as indicated by the low oxidant concentration around the electrode for lower oxidant concentration (Fig. 4, AR 4, $10 \mu\text{L min}^{-1}$, 20 mM vs. 144 mM). This increased oxidant consumption at lower concentration also explains the observed mass transport limitation and resulting decreased fuel cell performance (Fig. 5, AR 4, $10 \mu\text{L min}^{-1}$, 20 mM).

4. Conclusions

We report a fully-coupled 3D numerical model for laminar flow fuel cells (LFFCs), which included all the transport processes and

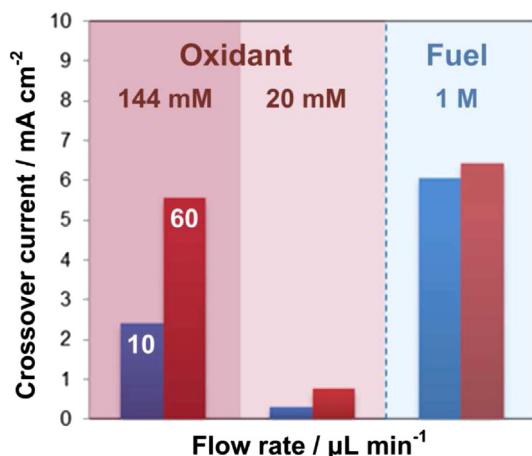


Fig. 8. Crossover current due to the oxidant and fuel reactant crossover for AR 4 structure operating at the lowest and highest reactant flow rate (10 and $60 \mu\text{L min}^{-1}$), lower and higher oxidant concentration (20 and 144 mM), and fuel concentration of 1 M HCOOH.

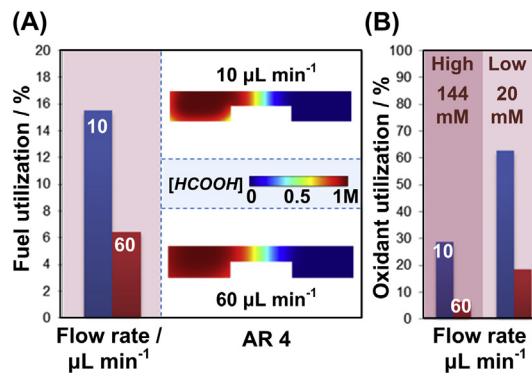


Fig. 9. (A) Fuel utilization and (B) Oxidant consumption rate for the AR 4 structure operating with 1 M HCOOH at the lowest and highest flow rates (10 and $60 \mu\text{L min}^{-1}$). Fuel utilization concentration captures are also provided for these flow rates, 9 mm downstream from the inlet (close to the outlet).

electrochemical phenomena that occur during the operation of fuel cells. The model coupled mass, momentum, species, and charge balances along with the Butler–Volmer equations for electrode kinetics. The model also included quantification of reactant utilization, reactant crossover and crossover current, and ancillary power losses associated with active reactant delivery. The model was validated using previous experimental data (I–V cell performance curves) obtained using a micro laminar flow fuel cell (μLFFC) with a bridge-shaped microchannel cross-section [13]. The cell performance predicted via modeling was in excellent agreement with the experimental data.

The model was used to study the effect of bridge geometry (aspect ratio), reactant flow rates, and oxidant concentration on various parameters characterizing the fuel cell performance. Higher concentration and higher flow rates will result in higher power densities, but higher crossover currents, lower fuel utilization and higher pressure-driven power losses. Higher aspect ratios of the bridge structure will lead to lower crossover currents, but lower power and higher pressure-driven power losses. Most of these correlations were attributed to the influence of the geometrical and operation parameters on the behavior of the depletion zone at the fuel–oxidant and reactant–electrode interfaces. For the various configurations studied here, we observed that the AR 4 bridge structure produced the higher power output ($\sim 49 \text{ mW cm}^{-2}$) when operated with 1 M HCOOH and 144 mM KMnO_4 at $60 \mu\text{L min}^{-1}$.

Although the actual performance numbers will depend on the specific fuel cell configuration, the trends predicted by the model will be applicable to various configurations of LFFCs. Based on the results here, we recommend the following design considerations:

1. If higher concentration of the oxidant can be used, then lower flow rates are desirable as higher values for peak power density along with higher fuel utilization can be obtained. Additionally, the lower flow rates will lead to lower pressure-driven power losses and lower crossover current. If higher concentrations of oxidants cannot be used, then the flow rate will need to be adjusted (using the developed numerical model) to obtain optimal performance with respect to power density, fuel utilization, power losses, and crossover currents.
2. The bridge-shaped microchannel cross-section enables (i) to reduce the fuel-to-oxidant interfacial contact thereby, minimizing reactant crossover and (ii) to isolate the evolving mixing zone from the reactive walls. Minimizing reactant crossover and separation of the mixing and reactions zones may increase reactant utilization and improve overall cell performance.

3. A lower aspect ratio for the bridge structure is desirable, as the peak power density will be higher and the pressure-driven power losses will be lower. The fuel crossover will be higher for low aspect ratio structure, but in our case the fuel crossover was only as high as 1.2% for the lowest aspect ratio structure.

The described model can be used to evaluate more complex configurations of the fuel cells along with experimental validation, e.g., a configuration where the electrodes are placed on the bridge wall to possibly increase fuel cell performance. Several previously reported experimental studies have insinuated that optimal placement of electrode can lead to enhanced fuel cell performance [1]. Similarly, the approaches for the modeling of laminar flow-based fuel cells reported in this manuscript can be used for broader applications, such as modeling of redox flow batteries (e.g., based on Vanadium-based redox couples) for enhanced understanding of the rate-limiting electrochemical steps.

Acknowledgments

We are grateful for the funding support from the Grainger Program at the University of Illinois, and the National Science Foundation (CAREER grant CTS 05-47617). We thank the personnel from the Micro-Nano-Mechanical Systems (MNMS) Cleanroom Laboratory, the Integrated Circuit (IC) Fabrication Laboratory, and the Imaging Technology Group (ITG) at the Beckman Institute for Advanced Science and Technology, University of Illinois, for their assistance.

Appendix A. Supplementary data

Supplementary data related to this article can be found at <http://dx.doi.org/10.1016/j.jpowsour.2014.06.127>.

References

- [1] E. Kjeang, N. Djilali, D. Sinton, J. Power Sources 186 (2009) 353–369.
- [2] S.A.M. Shaegh, N.-T. Nguyen, S.H. Chan, Int. J. Hydrogen Energy 36 (2011) 5675–5694.
- [3] S.J. Lee, A. Chang-Chien, S.W. Cha, R. O'Hayre, Y.I. Park, Y. Saito, F.B. Prinz, J. Power Sources 112 (2002) 410–418.
- [4] K.-B. Min, S. Tanaka, M. Esashi, J. Micromech. Microeng. 16 (2006) 505.
- [5] S. Motokawa, M. Mohamedi, T. Momma, S. Shoji, T. Osaka, Electrochem. Commun. 6 (2004) 562–565.
- [6] M. Shen, S. Walter, M.A.M. Gijs, J. Power Sources 193 (2009) 761–765.
- [7] S. Tominaka, S. Ohta, H. Obata, T. Momma, T. Osaka, J. Am. Chem. Soc. 130 (2008) 10456–10457.
- [8] Z. Xiao, C. Feng, P.C.H. Chan, I.M. Hsing, Sens. Actuators B: Chem. 132 (2008) 576–586.
- [9] J. Yeom, G.Z. Mozsgai, B.R. Flachsbarth, E.R. Choban, A. Asthana, M.A. Shannon, P.J.A. Kenis, Sens. Actuators B: Chem. 107 (2005) 882–891.
- [10] J. Yu, P. Cheng, Z. Ma, B. Yi, Electrochim. Acta 48 (2003) 1537–1541.
- [11] M. Frank, G. Erdler, H.P. Frerichs, C. Muller, H. Reinecke, J. Power Sources 181 (2008) 371–377.
- [12] C.W. Moore, J. Li, P.A. Kohl, J. Electrochem. Soc. 152 (2005) A1606–A1612.
- [13] P.O. Lopez-Montesinos, N. Yossakda, A. Schmidt, F.R. Brushett, W.E. Pelton, P.J.A. Kenis, J. Power Sources 196 (2011) 4638–4645.
- [14] E.R. Choban, L.J. Markoski, A. Wieckowski, P.J.A. Kenis, J. Power Sources 128 (2004) 54–60.
- [15] E.R. Choban, L.J. Markoski, J. Stoltzfus, J.S. Moore, P.J.A. Kenis (Eds.), Power Sources Proceedings, 2002, pp. 317–320.
- [16] M.-H. Chang, F. Chen, N.-S. Fang, J. Power Sources 159 (2006) 810–816.
- [17] R.S. Jayashree, L. Gancs, E.R. Choban, A. Primak, D. Natarajan, L.J. Markoski, P.J.A. Kenis, J. Am. Chem. Soc. 127 (2005) 16758–16759.
- [18] S.A.M. Shaegh, N.-T. Nguyen, S.H. Chan, J. Micromech. Microeng. 20 (2010) 105008.
- [19] M.H. Sun, G. Velasco Casquillas, S.S. Guo, J. Shi, H. Ji, Q. Ouyang, Y. Chen, Microelectron. Eng. 84 (2007) 1182–1185.
- [20] S.K. Yoon, G.W. Fichtl, P.J.A. Kenis, Lab Chip 6 (2006) 1516–1524.
- [21] D.H. Ahmed, H.B. Park, H.J. Sung, J. Power Sources 185 (2008) 143–152.
- [22] A. Bazylak, D. Sinton, N. Djilali, J. Power Sources 143 (2005) 57–66.
- [23] A.E. Khabbazi, M. Hoorfar (Eds.), ASME 2010 8th International Conference on Fuel Cell Science, Engineering and Technology, Brooklyn, New York, USA, 2010, pp. 659–665.
- [24] A.E. Khabbazi, A.J. Richards, M. Hoorfar, J. Power Sources 195 (2010) 8141–8151.
- [25] D. Krishnamurthy, E.O. Johansson, J.W. Lee, E. Kjeang, J. Power Sources 196 (2011) 10019–10031.
- [26] H. Wang, D.Y.C. Leung, J. Xuan, Int. J. Hydrogen Energy 36 (2011) 14704–14718.
- [27] J. Xuan, D.Y.C. Leung, M.K.H. Leung, H. Wang, M. Ni, J. Power Sources 196 (2011) 9391–9397.
- [28] J. Xuan, D.Y.C. Leung, H. Wang, M.K.H. Leung, B. Wang, M. Ni, Appl. Energy 104 (2013) 400–407.
- [29] G.E. Archie, AAPG Bull. 31 (1947) 350–366.
- [30] G.E. Archie, AAPG Bull. 34 (1950) 943–961.
- [31] S.P. Suter, R. Skalak, Annu. Rev. Fluid Mech. 25 (1993) 1–20.